International Journal of Multiphase Flow 200 (2026) 105725

Contents lists available at ScienceDirect

International Journal of Multiphase Flow

journal homepage: www.elsevier.com/locate/ijmulflow

Research Paper

PLIC-based contact line modeling for simulations of droplet impact onto smooth and structured surfaces

Jonathan Wurst [a,*], Maximilian Dreisbach [b], Alexander Stroh [b], Jochen Kriegseis [b], Kathrin Schulte [a]

[a] Institute of Aerospace Thermodynamics, University of Stuttgart, Pfaffenwaldring 31, Stuttgart, 70569, Germany
[b] Institute of Fluid Mechanics, Karlsruhe Institute of Technology, Kaiserstraße 10, Karlsruhe, 76131, Germany

ARTICLE INFO

Dataset link: https://doi.org/10.18419/DARUS-5496, Replication Data for: PLIC-based contact line modeling for simulations of droplet impact onto smooth and structured surfaces (Original data)

Keywords:
Volume-of-Fluid (VoF)
Dynamic contact angle
Structured surface
Droplet impact

ABSTRACT

We present a robust combination of methods for a Volume-of-Fluid (VoF) framework to investigate the influence of wettability on droplet impact onto grooved surfaces, with a particular focus on under-studied hydrophilic cases. The numerical method employs a three-phase PLIC interface reconstruction and utilizes the method of Sussman (2001) to model the contact line. This approach is shown to be compatible with both the balanced Continuum Surface Force (b-CSF) and Continuum Surface Stress (CSS) surface tension models. A mesh-dependent dynamic contact angle model based on Cox's theory is implemented, demonstrating improved grid convergence over standard no-slip conditions. The framework is validated extensively against analytical solutions for sessile drops and static menisci, as well as new experimental data for droplet impacts on both smooth and grooved surfaces. The simulations successfully reproduce the experimental spreading dynamics, though we also highlight significant discrepancies between commonly used dynamic contact angle models and experimental measurements, especially during the receding phase. Finally, a parameter study varying the contact angle from 10° to 150° reveals that spreading transversal to the grooves is almost independent of wettability. Conversely, spreading parallel to the grooves is strongly affected by wettability, behaving similarly to spreading on a smooth substrate. In accordance with theory, it is found that at contact angles of 45° and below, corner flow governs the spreading inside the grooves.

1. Introduction

Droplet impact is a prevalent and fundamental process in many applications. These include ink-jet printing, fuel injection, pesticide application, spray cooling (Deng and Gomez, 2011), and self-cleaning surfaces (Neinhuis, 1997). Early investigations on droplet impacts even date back to the 19th century (Worthington, 1876). Much of the research done concentrated on predicting the maximum spreading after impact (Scheller and Bousfield, 1995; PasandidehFard et al., 1996; Ukiwe and Kwok, 2004; Clanet et al., 2004; Roisman, 2009; Eggers et al., 2010; Mao et al., 1997) or the splashing threshold (Mundo et al., 1995; Stow and Hadfield, 1981; Cossali et al., 1997; Range and Feuillebois, 1998; Foltyn et al., 2022), two very important parameters for a practical design.

A frequently overlooked parameter is the wettability, which in general describes the affinity of a liquid to create a solid–liquid interface. If the liquid–gas interface is energetically more favorable, the liquid will barely wet the surface and the wettability is superhydrophobic. If the liquid–solid interfacial region strongly decreases the interfacial energy, the liquid will completely spread on this superhydrophilic surface. All states in between can be called partially wettable. The region where the three phases liquid, solid, and gas meet is the contact line. The contact angle θ is a theoretical concept to indicate the degree of wettability, with $\theta < 90°$ called hydrophilic and $\theta > 90°$ hydrophobic. On ideal surfaces, the true equilibrium contact angle can be calculated by Young's equation (Young, 1805). On rough and chemically heterogeneous surfaces, which applies to every real surface, there are also metastable contact angles in between the contact angle hysteresis interval (Marmur et al., 2017). This interval is limited by the advancing θ_{adv} and receding θ_{rec} contact angles, the greatest and smallest values observable before the contact line starts to move. A contact line movement is accompanied by a change of the apparent contact angle, which usually needs to be modeled. Dynamic contact angle models describe the dependence of the contact angle on the contact line velocity and can be used for this purpose.

A unidirectional surface modification similar to a grooved substrate is a chemically patterned surface on which hydrophobic and

* Corresponding author.
E-mail address: jonathan.wurst@itlr.uni-stuttgart.de (J. Wurst).

https://doi.org/10.1016/j.ijmultiphaseflow.2026.105725
Received 8 November 2025; Received in revised form 12 February 2026; Accepted 2 April 2026
Available online 5 April 2026

hydrophilic stripes alternate. The final states of micro-droplets impacting onto surfaces with stripe widths that are one order of magnitude smaller than or of the same order of magnitude as the droplet diameter were investigated by Léopoldès et al. (2003). For droplets of the same size, they found that the resulting shape is highly elongated, whereas for much smaller stripes, the droplet shape was always almost circular. The intermediate sizes produced shapes described as "lozenge" and "butterfly", depending on the impact position. Jansen et al. (2012) varied the kinetic energy and observed final shapes that were stretched perpendicular to the stripes with an aspect ratio smaller than one, compared to low kinetic energy impacts, where the resulting shape is strongly elongated along the stripes. Wang et al. (2019) studied numerically the droplet impact onto a chemically striped surface and found that the influence of the stripe pattern is negligible at high impact speeds in terms of maximum spreading. Such a patterned surface can also generate secondary droplets, which was investigated numerically by Zou et al. (2023). They were able to show that there is an optimal number of stripes that a drop must cover at maximum spreading in order to achieve maximum generation of secondary droplets.

In difference to a chemically patterned surface, a grooved substrate adds the uncertainty of inaccurate edges or uneven surface qualities as well as resolution requirements inside the grooves and an involved interface reconstruction at the groove edges. But the dynamics and outcome of a droplet impact can also be changed significantly when adding a structure to the solid surface (Lin et al., 2019; Kannan and Sivakumar, 2008; Fink et al., 2018). With the right choice of structures and wettability, a given process can be directed towards a favored regime, as demonstrated for example by Fink et al. (2018). They showed that under the same impact conditions the outcome can shift from deposition for a smooth surface to bouncing on micro-grooves. With current technologies a broad spectrum of possibilities for such structures is available. They allow alterations down to the nanoscale and a variety of different structure types like cylindrical pillars (Tümer et al., 2022), cubic or pyramidal structures (Palmetshofer et al., 2024), and grooves (Kannan and Sivakumar, 2008). The latter is of particular interest due to its comparatively simple fabrication process and its ability to promote rebound and non-wetting states on hydrophobic surfaces (Fink et al., 2018; Malla et al., 2017). These are essential in popular applications like anti-icing, self-cleaning or drag-reduction designs. Numerically, Hu et al. (2022) investigated the bouncing behavior on superhydrophobic grooves and achieved good agreement with the experiment despite applying only a static contact angle. They eventually proposed design principles to establish so called pancake bouncing, a rebound without a retraction phase. The cause for the transition between complete bouncing and bouncing with droplet breakup is the impalement transition from non-wetting (Cassie-Baxter) to wetting (Wenzel) state, as previously shown experimentally by Malla et al. (2017). Investigations with the focus on bouncing are thus a very prominent subject in the literature (Liu et al., 2014; Hu et al., 2022; Guo et al., 2018; Malla et al., 2017; Fink et al., 2018). The spreading after impact occurs anisotropically due to the nature of the grooves. Vaikuntanathan and Sivakumar (2016) reported a rise of anisotropy in their experiments when increasing the Weber number. Conversely, Malla et al. (2017) observed the opposite, a decrease of the directional dependence for higher impact conditions. The effect of the groove geometry was also the focus of the recent study by Huang et al. (2025), but the anisotropy was not investigated further.

One of the drawbacks of experimental studies can be clearly observed on this subject. Almost all studies investigated the effect of Weber number and the groove geometry on the process (Malla et al., 2017; Vaikuntanathan and Sivakumar, 2016; Kannan and Sivakumar, 2008; Guo et al., 2018; Huang et al., 2025; Hu et al., 2022; Jin and Wang, 2020), most likely because changing the wettability involves either manufacturing of new samples with a different material or intricate treatment of the substrates. Moreover, the research focused on hydrophobic and superhydrophobic substrates. With such characteristics, applications like self-cleaning or anti-icing surfaces are the subject of interest. Beyond that, textured surfaces can also be used in applications like spray cooling (Zhang and Wang, 2015). Installing a grooved surface to improve heat transfer requires a good wettability. It is therefore crucial to understand how such hydrophilic surfaces are wetted when droplets hit them. We hence studied numerically the droplet impact onto surfaces with varying wettability and a particular focus is set on hydrophilic surfaces, as these have hardly been studied to date. It is then shown how the wettability affects the anisotropy during spreading.

To simulate droplet impacts, the contact line dynamics play an important role and still remains challenging for a numerical simulation. Droplet impacts onto a structured surface feature merging and breakup processes, for which the Volume of Fluid (VoF) method is particularly suitable. Additionally, for conserving a sharp interface, the piecewise linear interface calculation (PLIC) method (Rider and Kothe, 1998) is state of the art. This work hence also aims to provide a contribution for a robust approach to deal with contact line dynamics based on the VoF and PLIC method.

Afkhami et al. (2009) proposed a contact angle modeling which is designed to cancel the effect of the numerical slip, responsible for poor convergence properties (Gründing et al., 2020). A framework for contact line movement in complex geometries was proposed by Pathak and Raessi (Pathak and Raessi, 2016b,a). They developed a PLIC method for three-phase cells and incorporated it in a VoF-scheme for two fluids and moving rigid bodies with the fictitious domain method. However, no contact angle was applied nor any other way to account for the wettability. Recently, Tavares et al. (2024) proposed a method for two-phase flows including contact line dynamics for complex surfaces, which was further improved by Chen et al. (2025). It is based on the accurate height-function method and uses the b-CSF model but there is no dynamic contact angle model applied and a static value is used instead. Göhl et al. (2018) used an immersed boundary method and compared different contact angle models to simulate droplet impacts onto complex surfaces. Their framework was based on the Continuum Surface Force (CSF) (Brackbill et al., 1992) formulation, known to be prone for spurious currents (Tryggvason et al., 2011). Patel et al. (2017) developed a framework and included the wettability with the method of Sussman (2001). In this method, the interface at the contact line is extrapolated into the solid phase according to the contact angle in order to take wettability into account when calculating the surface tension force. As dynamic contact angle model they applied the Hoffman–Voinov–Tanner law (Kistler, 1993) and also the CSF model for the surface tension calculation. Unlike Göhl et al. and the presented framework, the solid boundaries were taken into account with an immersed boundary method. The method of Sussman was also used by several more groups, e.g. Yokoi (Yokoi et al., 2009; Yokoi, 2013), Sun and Sakai (Sun and Sakai, 2015, 2016), and Kuipers (Patel et al., 2017; Das et al., 2018; Milacic et al., 2019).

In order to capture the contact line dynamics in the simulation, our approach also employs Sussman's method and combines it with other methods for interface reconstruction and dynamic contact angles in Section 2. We conducted experiments for the validation and evaluated the dynamic contact angle as input for the simulation. The experimental setup and procedure thereof is described in Section 3. The framework is validated in Section 4 and numerical investigations about droplet impact onto hydrophilic grooves are presented in Section 5.

2. Numerical methods

We implemented the methods in the in-house code *Free Surface 3D* (FS3D) (Eisenschmidt et al., 2016), a multiphase flow solver developed and optimized for Direct Numerical Simulations of droplet and spray interactions as well as phase change processes. Following the

initial development by Rieber (2004), the methodology has been subsequently advanced by further research. FS3D solves the incompressible Navier–Stokes equations

$$\nabla \cdot \mathbf{u} = 0, \tag{1}$$

$$\rho \left[\frac{\partial \mathbf{u}}{\partial t} + \nabla \cdot (\mathbf{u} \otimes \mathbf{u}) \right] = \nabla \cdot (\mathbf{S} - \mathbf{I}p) + \rho \mathbf{g} + \mathbf{f}_\sigma, \tag{2}$$

where $\mathbf{u}$ denotes the velocity vector, ρ the local density, p the pressure and $\mathbf{g}$ the gravitational acceleration. The additional term $\mathbf{f}_\sigma$ describes the resulting force of the surface tension σ acting only at interfaces and is dealt with in more detail in Section 2.2. For a Newtonian fluid, the shear stress tensor $\mathbf{S}$ is given by

$$\mathbf{S} = \mu \left[\nabla \mathbf{u} + (\nabla \mathbf{u})^T \right] \tag{3}$$

where μ stands for the dynamic viscosity. The system is discretized with the Finite Volume method on a Cartesian grid and employs the Marker and Cell method (Harlow and Welch, 1965). Velocity components are therefore stored on cell faces, while scalar variables like pressure and density are located in the cell centers. A second order upwind scheme is used to discretize the momentum advection. The fluxes are solved applying a second-order Godunov method and a Total Variation Diminishing (TVD) limiter (van Leer, 1979) with a Strang-splitting scheme (Rieber, 2004). As the flow is considered incompressible, the pressure is coupled only implicitly by the Poisson equation

$$\nabla \cdot \left[\frac{1}{\rho} \nabla p \right] = \nabla \cdot \left[-\nabla \cdot (\mathbf{u} \otimes \mathbf{u}) + \frac{1}{\rho} \left(\nabla \cdot \mathbf{S} + \rho \mathbf{g} + \mathbf{f}_\sigma \right) \right] \tag{4}$$

and is solved in a separate step using a multi-grid scheme with the Gauss–Seidel algorithm as the smoother (Rieber, 2004; Wesseling, 1992). To distinguish between the different phases, the phase distribution is tracked with the Volume-of-Fluid (VoF) method (Hirt and Nichols, 1981) by introducing a scalar variable

$$f(\mathbf{x}, t) = \begin{cases} 0 & \text{inside the gas phase,} \\ (0, 1) & \text{in interface cells,} \\ 1 & \text{inside the liquid phase.} \end{cases} \tag{5}$$

The transport equation for f

$$\frac{\partial f}{\partial t} = -\nabla \cdot (f \mathbf{u}) \tag{6}$$

is solved by applying the piecewise linear interface calculation (PLIC) (Rider and Kothe, 1998) with a Strang-splitting approach (Strang, 1968). Details of the reconstruction are given in Section 2.1. Using the VoF-variable, a fluid property φ is calculated in the one-field formulation via $\varphi(\mathbf{x}, t) = \varphi_g + f(\mathbf{x}, t)(\varphi_l - \varphi_g)$, where φ_g and φ_l are the properties of the gas and liquid phase, respectively.

Two different surface tension models are implemented in FS3D and applied in this study. One is the balanced Continuum Surface Force model (b-CSF) by Popinet (2009), that adds a balanced force approach to the CSF model by Brackbill et al. (1992). Besides the balanced formulation, an improved curvature calculation is used employing the height functions (Popinet, 2009). The second is the Continuum Surface Stress model (CSS) by Lafaurie et al. (1994) with modifications by Steigerwald et al. (2024). The b-CSF is in general regarded as the better choice (Albert et al., 2012), but the implementation can be quite involved and the scheme is prone to problems at low resolutions. Also merging or breakup processes are delicate without a fallback strategy. The CSS, on the other hand, is not as accurate and higher spurious currents can be observed, but it easily handles low resolutions. Moreover, the method has been extensively validated within the FS3D framework for applications involving large topology changes, demonstrating superior robustness. Furthermore, compared to the b-CSF, it benefits more from the GPU-accelerated hardware that we use on the supercomputer.

The solid phase in the case of a structured surface is represented by a rigid body framework (Rauschenberger and Weigand, 2015) that is based on the work of Patankar et al. (2000). All the solid interfaces are consistently positioned on cell faces.

2.1. Interface reconstruction

The interface is reconstructed based on the PLIC method. A plane is positioned in the cell such that it divides the cell volume according to the local VoF value and is described with a normal vector $\mathbf{n}_f$ and a displacement parameter l^*. In the method of Youngs (1984), the normal of the PLIC-plane is set by the gradient of the VoF variable

$$\mathbf{n}_Y = -\nabla f. \tag{7}$$

Next to a wall boundary with the normal $\mathbf{n}_w$, there is no full stencil available required for the gradient calculation. In this situation, the reconstruction developed by Potyka and Schulte (2024) is applied. The normal obtained by the method of Youngs $\mathbf{n}_Y$ serves as an input to extract the vector $\mathbf{t}_f$ as

$$\mathbf{t}_f = \frac{\mathbf{n}_Y - (\mathbf{n}_w - \mathbf{n}_Y)\mathbf{n}_w}{\left| \mathbf{n}_Y - (\mathbf{n}_w - \mathbf{n}_Y)\mathbf{n}_w \right|}, \tag{8}$$

which is the orientation of the interface tangential to the wall. The actual normal can then be represented by Patel et al. (2017)

$$\mathbf{n}_f = \mathbf{n}_w \cos(\phi) + \mathbf{t}_f \sin(\phi) \tag{9}$$

with the angle ϕ towards the solid surface. This angle is found by minimizing an objective function $h(\phi)$ that describes how well the orientation matches also the fluid distribution in neighboring cells. It can be written as

$$h_{ijk}(\phi) = \sum_{i^*=i-1}^{i+1} \sum_{j^*=j-1}^{j+1} \sum_{k^*=k-1}^{k+1} \left(\tilde{f}_{i^* j^* k^*}(\phi) - f_{i^* j^* k^*} \right)^2 \tag{10}$$

where $\tilde{f}$ describes the predicted VoF value when extending the PLIC plane in the neighboring cell. This approach is applied for interface cells located next to the solid boundary. It also enables the reconstruction at the contact line without imposing any predetermined contact angle. However, the PLIC angle towards the solid phase differs from the contact angle used for the Sussman method and thus for surface tension. Simulations showed that, as a result, the interface spread and widened over several cells, thereby losing its sharpness. To avoid this, the angle ϕ is set to the contact angle in cells containing the interface.

2.2. Contact line dynamics

The surface tension force $\mathbf{f}_\sigma$ at a solid boundary has to be calculated according to the contact angle. On an ideal smooth surface, the contact angle is well defined by Young's equation (Young, 1805), which relates the three interfacial tensions to the contact angle θ. However, the interfacial tensions are difficult to obtain and additionally a real solid surface is never ideally smooth and/or chemically homogeneous. For real systems, the angle is referred to as apparent contact angle and is in practice measured for each system. Still, the measured angle can in principle be any value between the advancing and receding contact angles (Marmur et al., 2017).

To represent the adhesion connected to a rigid wall, in simulations usually the no-slip condition is enforced. Although this leads to the paradox of a non-moving contact line (Huh and Scriven, 1971), with a staggered velocity arrangement the problem is overcome. However, an implicit slip is introduced that depends on the grid size and hence leads to slow convergence properties (Renardy et al., 2001; Gründing et al., 2020; Afkhami et al., 2009; Tavares et al., 2024). It has been shown that using a Navier-slip condition can solve this problem when the associated slip length is resolved by the grid sufficiently (Gründing et al., 2020; Tavares et al., 2024).

2.2.1. Contact angle boundary condition

At a solid boundary, no full stencil is available for the surface tension force calculation. To provide the absent stencil, the method

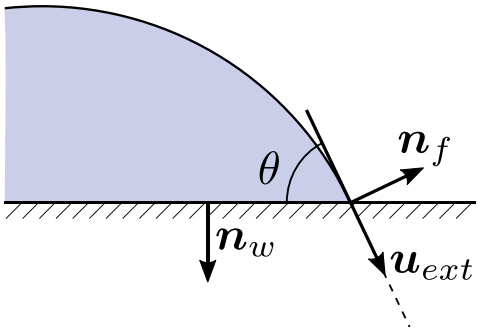

Fig. 1. Sketch of the method by Sussman (2001). The extension velocity $\mathbf{u}_{ext}$ is constructed to transport the liquid according to the contact angle θ into the ghost cells.

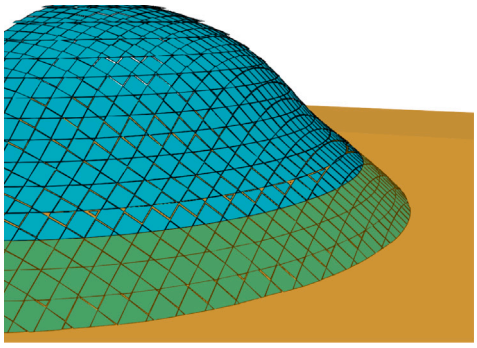

Fig. 2. PLIC representation of the extended VoF field after setting the contact angle boundary condition. The ghost cells are visible inside the translucent solid phase.

of Sussman (2001) is applied. It was originally formulated for the level-set approach and similar to Patel et al. (2017) we apply it here within the PLIC method. The basic idea is sketched in Fig. 1. The approach creates a boundary condition for the VoF field with the help of an artificial velocity field $\mathbf{u}_{ext}$. The wall normal $\mathbf{n}_w$ as well as the PLIC-normal $\mathbf{n}_f$ are known, and hence the extension velocity can be constructed by Sussman (2001)

$$\mathbf{u}_{ext} = \frac{\mathbf{n}_w + \cot(\theta)\mathbf{n}_2}{\left|\mathbf{n}_w + \cot(\theta)\mathbf{n}_2\right|}, \tag{11}$$

$$\mathbf{n}_2 = -\frac{\mathbf{n}_1 \times \mathbf{n}_w}{\left|\mathbf{n}_1 \times \mathbf{n}_w\right|}, \tag{12}$$

$$\mathbf{n}_1 = -\frac{\mathbf{n}_f \times \mathbf{n}_w}{\left|\mathbf{n}_f \times \mathbf{n}_w\right|}, \tag{13}$$

with the auxiliary vectors $\mathbf{n}_1$ and $\mathbf{n}_2$, which lie in the wall plane tangential and normal to the contact line, respectively. Note that the wall normal in cells adjacent to a groove edge is averaged with neighboring cells, thus creating a smoother transition of the contact line across three cells of the groove edge. Because of the sharp interface, the artificial velocity can only be constructed in interface cells. We were able to significantly improve the resulting VoF values in the ghost cells by making use of a smoothed VoF distribution such that also in neighboring cells the velocity can be constructed. Using this artificial velocity field, a few steps of the transport scheme are performed with an artificial time step (Yokoi et al., 2009; Patel et al., 2017) of $\Delta\tilde{t} = 0.5\Delta z|\mathbf{u}_{ext}|^{-1}$, which proved to be a robust choice for a wide range of contact angles tested. The interface has to be reconstructed inside the ghost cells after every pseudo-advection step, while inside the simulation domain the original state is restored. After an efficient number of steps, the volume fractions in the ghost cells remain constant, which in this study is monitored with the sum of volume fractions over all ghost cells. If the relative change of this sum falls below a threshold of 10^{-3}, the iteration is stopped. Choosing for example the CSS model, the surface tension force is calculated by

$$\boldsymbol{f}_\sigma = \sigma\nabla\cdot|\nabla f|\left(\boldsymbol{I} - \boldsymbol{n}_f \otimes \boldsymbol{n}_f\right). \tag{14}$$

As in total the second derivative is needed and the gradients are approximated by central differences, at least two layers of ghost cells are needed. Additionally, in the CSS model, the VoF field is smoothed beforehand and thus at least one more layer is required. An exemplary result of the extended VoF field is depicted in Fig. 2. A snapshot of a spreading drop test case is shown with an imposed contact angle of $\theta = 40°$ and a PLIC reconstruction of the VoF distribution also inside the solid phase. An advantage of constructing such an extended VoF field is the flexibility with regard to the surface tension model. The surface tension models themselves do not need to be adjusted to incorporate the wettability and the model can be easily changed depending on simulation requirements.

2.2.2. Contact angle hysteresis

The contact angle hysteresis describes the effect a non-ideal surface has on the contact angle. A contact line with a contact angle in between the interval of the advancing θ_{adv} and receding θ_{rec} contact angles (Marmur et al., 2017) remains pinned. This becomes relevant for droplet impacts with a receding phase, because the transition between spreading and retracting is affected by pinning. To capture the contact angle hysteresis on smooth surfaces, an algorithm by Linder et al. (2015) is applied. The idea is that when keeping the boundary condition of the VoF distribution fixed, the resulting surface force will prevent the contact line from moving. This means that the boundary condition, usually representing some form of gradient of the VoF variable, will change from a Neumann condition to a Dirichlet condition and retains its value. Since the contact angle boundary condition is set globally, also the pinning is enforced over the complete contact line. The approach is therefore not suitable for the simulation of complex phenomena where only part of the contact line is pinned as it is the case for a droplet impact onto grooves. Simulations of the latter are conducted without an explicit pinning but by considering the hysteresis interval in the dynamic contact angle model. Note also, that this approach seems to work only for the sharp interface modeling of the b-CSF, while for the CSS, where a smoothing is applied, we observed that the contact line is still able to move. Thus, we are applying this method only for the droplet impact onto a smooth surface in Section 4.3 together with the b-CSF model.

2.2.3. Dynamic contact angle model

The contact angle of a moving contact line θ_{dyn} differs from the static contact angle θ_Y and is a function of the capillary number $\mathrm{Ca} = u_{cl}\mu/\sigma$, which can be seen as a dimensionless contact line velocity u_{cl}. This is usually expressed with a contact angle model. Besides many empirical correlations, there are also more fundamental theories available. Cox' very prominent hydrodynamic theory (Cox, 1986) matches asymptotic solutions for the interface slope on different length scales. In that way he could bridge the capillary-driven micro-scale to the inertia-driven macro-scale. Due to the different scales, refining the grid size around the contact line leads to mesh-dependent solutions (Gründing et al., 2020; Renardy et al., 2001). Following the idea of Afkhami et al. (2009), Cox' theory is here used to apply a mesh-dependent contact angle. This way, the changing contact angle counteracts the effect of an implicit slip. For an advancing contact line, e.g., when refining the grid, the contact angle decreases, according to Cox' theory, and accelerates the contact line. At the same time, with the grid refinement also the viscous stress increases because the no-slip condition is fulfilled slightly better. Mathieu's model is a polynomial approximation of Cox' theory and valid for fluids with a high viscosity ratio as for water and air and

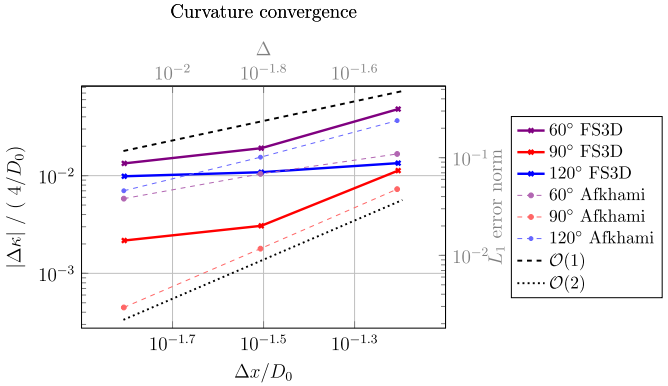

Fig. 3. Grid convergence of the normalized error between the averaged curvature at the contact line and the analytic value $|\Delta\kappa|$ for three different contact angles. On the right and top axis, the results of Afkhami and Bussmann (2008) are shown for comparison.

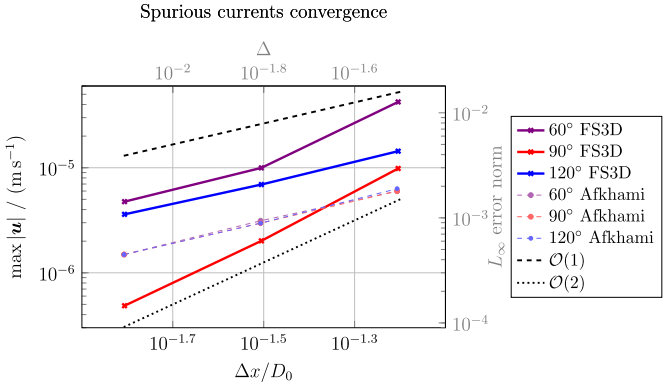

Fig. 4. Grid convergence of the spurious currents for three different contact angles. On the right and top axis, the results of Afkhami and Bussmann (2008) are displayed for comparison.

is given by Mathieu (2003)

$$\theta_{dyn} = g^{-1}\left(g(\theta_{st}) + \mathrm{Ca}\ln\left(\frac{r_0}{\lambda}\right)\right), \tag{15}$$

$$g(\theta) = \frac{1}{9}\theta^3 - 0.00183985\theta^{4.5} + 1.845829\cdot 10^{-6}\theta^{12.258487}, \tag{16}$$

$$g^{-1}(\theta) = (9\theta)^{1/3} + 0.07273787\theta - 0.05153880\theta^2 + 0.00341336\theta^3, \tag{17}$$

with the outer length scale r_0, on which the contact angle is applied and thus set to half the grid spacing (Göhl et al., 2018; Legendre and Maglio, 2013) $r_0 = 0.5\Delta z$, and the slip length λ, which is set to a physical reasonable value of $\lambda = 1\,\mathrm{nm}$ (Göhl et al., 2018; Dupont and Legendre, 2010). The static value θ_{st} is set to the advancing θ_{adv} or receding contact angle θ_{rec} depending on the direction of movement.

2.3. Convergence tests

The implementation of the contact angle boundary condition is tested with three convergence tests applying the more accurate b-CSF model and the height function approach. These comprise three sensitive quantities to compute at the contact line. The first two tests evaluate the curvature and spurious currents of a sessile drop with diameter D, analogously to Renardy and Renardy (2002) and Afkhami and Bussmann (2008) and show comparable convergence rates. In the third test, the convergence of the contact line movement is investigated.

2.3.1. Curvature at contact line

The accuracy of the curvature is crucial for capillary driven flows. Especially along the contact line, the errors can drastically increase and are investigated in this test. The mean curvature along the contact line is compared to the analytic value $4/D_0$ for a sessile drop with three different contact angles. Following Afkhami and Bussmann (2008), the Ohnesorge number is set to $\mathrm{Oh} = \mu/\sqrt{\rho D_0 \sigma} \approx 1.15$ ($\mu = 0.1\,\mathrm{Pa\,s}, \rho = 400\,\mathrm{kg\,m^{-3}}, D_0 = 5\,\mathrm{mm}, \sigma = 3.57\,\mathrm{mN\,m^{-1}}$). The convergence with grid refinement of the normalized error between the averaged curvature at the contact line and the analytic value is shown in Fig. 3. For all contact angles, the errors are converging. $\theta = 90°$ is close to a first-order decay while $\theta = 60°$ converges slightly slower and $\theta = 120°$ shows the slowest convergence. On the right and top axis and in pale colors, also the results of Afkhami and Bussmann (2008) are displayed for comparison. Note that the absolute values cannot be compared, as it is not clear what reference units were chosen. The convergence rate is very similar for $\theta = 60°$, however, it is better for the other two angles.

2.3.2. Spurious currents

Spurious currents are a well-known numerical artifact that arise at the interface and also at the contact line. The same test case as above is used where ideally the result is a zero velocity field. The maximal velocity is therefore evaluated for the same three contact angles. The convergence of the spurious currents is shown in Fig. 4. For $\theta = 90°$, they converge at a second-order rate and for the other two angles slightly faster than first-order. Again, on the right and top axis and in pale colors, the results of Afkhami and Bussmann (2008) are presented for comparison. They converge on a first-order rate and therefore slightly worse. It should be noted, though, that Afkhami and Bussman did not wait until equilibrium was reached, but ended the simulation after 100 time steps.

2.3.3. Moving contact line

As mentioned in Section 2.2, simulations of moving contact lines with the no-slip condition exhibit slow convergence properties without any special treatment (Afkhami et al., 2009; Gründing et al., 2020; Renardy et al., 2001; Tavares et al., 2024). In a staggered velocity arrangement, the velocity next to the wall is not zero and introduces an implicit slip which is grid dependent. In this test case, a drop in contact with the wall is released and spreads towards the equilibrium shape. The Ohnesorge number is set to $\mathrm{Oh} \approx 0.035$ ($\mu = 10\,\mathrm{mPa\,s}, \rho = 1000\,\mathrm{kg\,m^{-3}}, D_0 = 2\,\mathrm{mm}, \sigma = 40\,\mathrm{mN\,m^{-1}}$). The diameter of the wetted area relative to the initial droplet diameter is the spreading factor $\beta = \frac{D}{D_0}$. Using the no-slip condition with a static contact angle, the maximum spreading factor β_{max} depends strongly on the resolution, as can be seen in Fig. 5 (black line), due to the aforementioned grid-dependent slip. The Navier-slip condition allows explicitly for a slip tangential to the wall

$$u_\parallel = \lambda \left.\frac{\partial u}{\partial z}\right|_{z=0}. \tag{18}$$

When using a slip length that can be resolved, the simulation result will converge (Gründing et al., 2020; Afkhami et al., 2009; Tavares et al., 2024). In Fig. 5, the same spreading drop test shows no grid dependence when using the Navier-slip condition. However, the applied slip length $\lambda = 125\,\mu\mathrm{m}$ is physically several orders of magnitude too large. A physical slip length cannot be resolved for macroscopic applications with the current hardware and code performance. The same spreading drop case is simulated with the contact angle model from Mathieu and is shown along with an empirical contact angle model by Kistler (1993) in Fig. 5. Similar to the static contact angle with no-slip condition, the results with Kistler's model depend on the resolution. Choosing Mathieu's model improves this behavior strongly.

3. Experiments

The parallel light focused shadowgraphy technique is used to acquire measurement data of the impinging droplets. This method pro-

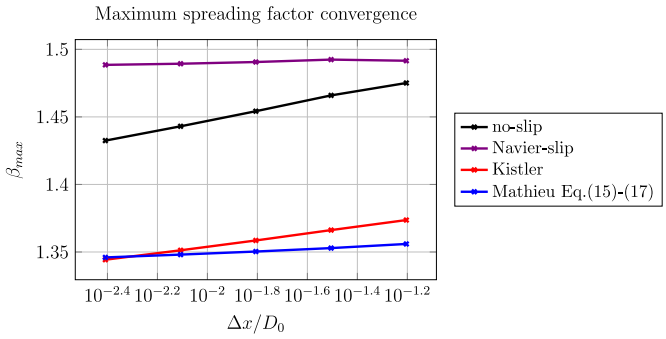

Fig. 5. Grid convergence for the maximum spreading factor of a spreading drop test case. The no-slip and Navier-slip case use a static contact angle and the Kistler and Mathieu case also employ the no-slip condition.

vides a sharp projection of the gas–liquid interface at high spatial resolution and, thus, facilitates precise capture of the droplet shape (Settles, 2001), allowing for the accurate measurement of the impact velocity, droplet diameter, contact line velocity, contact angle, and contact angle hysteresis. The perpendicular impingement of droplets consisting of different fluids (water and isopropanol) at varying impact velocities on smooth and structured substrates made of different materials is investigated. In the following paragraphs, the experimental setup and image processing procedure are described in rough detail, more information can be found in Dreisbach (2025).

3.1. Experimental setup

In order to investigate the anisotropic wetting of structured substrates, an additional bottom view using the principle of transmitted light shadowgraphy is implemented alongside the classical lateral view operated in the reflected light shadowgraphy. The measurement setup for the simultaneous imaging of the impinging droplet from the side and below is illustrated in Fig. 6. The droplet is illuminated by two high-power *ILA_5150 LPSv3* LEDs with narrow-banded spectra and maxima in the visible spectrum at $\sim 455\,\text{nm}$ and $\sim 632\,\text{nm}$, producing blue and red illumination, respectively. As illustrated in Fig. 6, the red light path is redirected by an assembly of two mirrors and a long-pass dichroic mirror with a cut-on wavelength at $\sim 567\,\text{nm}$. Consequently, the red light is reflected at the dichroic mirror, whereas the blue light is transmitted. A *Photron Nova R2* high-speed RGB camera simultaneously captures both views in the corresponding red and blue color channels, allowing subsequent separation into two independent perspectives of the droplet. The camera is equipped with a *Schneider-Kreuznach Apo-Componon* 4.0/60 enlarging lens and operates at a frame rate of $f = 7,500$ frames per second (fps) and $1280\,\text{px} \times 512\,\text{px}$ resolution. The high power of the LED illumination allows for short exposure times of $2.8 - 5\,\mu\text{s}$, thereby minimizing motion blur. An optical collimator consisting of a pinhole aperture and a biconvex lens is placed between the backlight and the droplet to produce a parallel light beam, ensuring precise imaging of the drop contour. An automated drop supply system, comprised of a syringe operated by a linear actuator, ensures reproducible droplet volume. The entire drop supply system can be adjusted in height, so that different impact velocities and thus a variation of the Reynolds and Weber numbers can be realized. The focal plane of the camera is aligned with the contour of sessile droplets after impingement, and the reproduction scale is measured with graph paper. Depending on the spreading factor of the droplets, an optimal field of view with regard to capturing the entire droplet in all frames, and simultaneously high resolution of the recorded droplet is determined, resulting in reproduction scales between $d_c = 106.67 - 278.26\,\text{px/mm}$ depending on impact velocity.

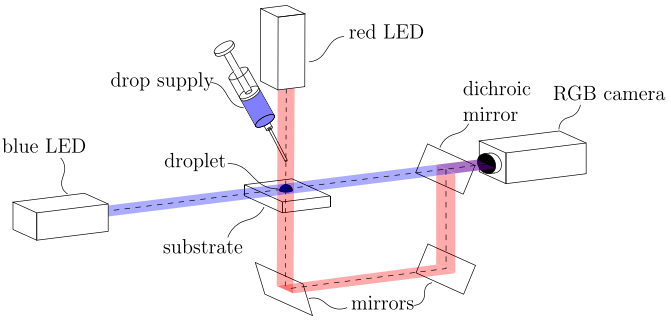

Fig. 6. Sketch of the test rig.
Source: adapted from Dreisbach et al. (2023).

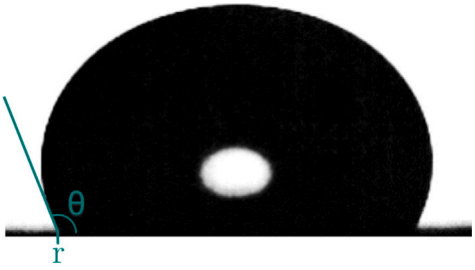

Fig. 7. Shadowgraph image of a droplet during impingement with overlayed measured contact angle θ and contact line position r.

3.2. Image processing

An image-processing algorithm was developed to determine impact velocity, droplet diameter, contact line velocity, contact angle, and contact angle hysteresis using image sequences recorded in the lateral view. In the first step, the contrast and brightness of the recorded grayscale images were adjusted and image noise was reduced by removing structures of dark pixels below a certain size. A processed image can be seen in Fig. 7. The substrate ground is detected by determining the maximum vertical gradient in the images calculated by a Sobel filter. The impact time is determined by detecting a change in the averaged pixel values in the bottom pixel row above ground, resulting from the appearance of the dark shadowgraphy contour. The droplet diameter is determined by the maximum width of the droplet measured in the two frames before impingement. During the experiments, an average droplet diameter $D_0 = 2.1\,\text{mm}$ was measured, resulting in a Bond number of $\text{Bo} = 0.15$. Due to the low Bond number, the drop shape can be regarded as approximately spherical. The impact velocity U_0 is determined by tracking the vertical displacement of the lower droplet boundary in the last two frames before impingement.

3.3. Parameter calculation

The contour of the droplet is detected in the images by gradient analysis. The Sobel filter is used to calculate the gradient distribution in the horizontal $grad_h$ and vertical $grad_v$ direction in the grayscale images. From the gradient distribution, the orientation α of the phase boundary is determined as

$$\alpha = \arctan\left(\frac{|grad_v|}{|grad_h|}\right). \tag{19}$$

The contact angles θ at the left and right contact lines are calculated as the average of the phase boundary orientation across the three image rows above ground. The positions of the left and right contact lines $r_{l,r}$ in each image are determined by the maximum horizontal gradient in the lowest image row. In order to obtain sub-pixel accuracy, the

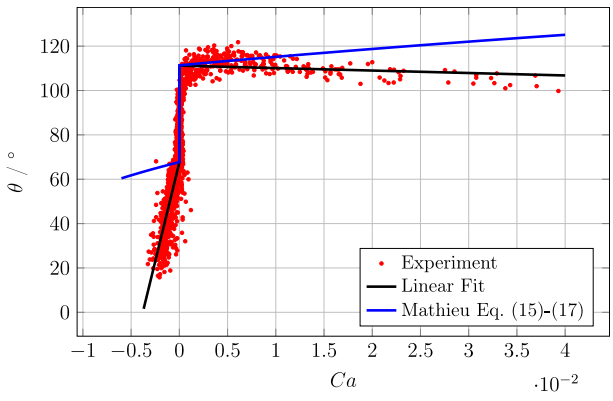

Fig. 8. Hoffman graph of the dynamic contact angle measurements for water droplet impacts onto a smooth polycarbonate substrate. Mathieu's model as well as a linear fit are shown as lines.

horizontal gradient distribution around the pixel with the maximum gradient magnitude is fitted with a second-order polynomial. The wetted diameter D is determined as the distance between r_l and r_r, from which the spreading factor can be calculated. The contact line velocity $u_{\mathrm{cl}} = \frac{\Delta r}{\Delta t}$ is determined by dividing the difference of the contact line positions Δr between two frames, by the time difference Δt.

The contact line dynamics can be visualized using a Hoffmann graph. In the Hoffmann graph, the contact angle θ is plotted against the capillary number Ca, which is a dimensionless representation of the contact line velocity. At Ca = 0, the contact angle hysteresis can be determined. Image noise and varying interface curvature during the dynamic deformation of the drop result in uncertainties in the measurement of contact angle and contact line velocity. The measurement error is estimated to be below ±2° for the contact angle and ±0.5 px for the contact line location. Consequently, a contact line displacement $\Delta r <$ 0.5 px is considered to be stationary and accordingly, the advancing and receding contact angles are determined from the Hoffmann graph. Fig. 8 shows the Hoffmann graph determined by the experiments of droplet impingement on the polycarbonate substrate. Additionally, the dynamic contact angle model by Mathieu Eq. (15)–(17) as well as a linear fit are displayed in the graph.

3.4. Experiments on droplet impact on smooth surfaces

Using the experimental setup, further information for the numerical description of the contact line dynamics is obtained in a parameter study for the deposition-like drop impact at different Reynolds and Weber numbers. The kinematic conditions of the drop impact are varied by changing the impact velocity, while different drop fluids (water and isopropanol) made it possible to influence the outcome of the drop impact via different material properties. In total, a range of $Re = 170 - 3100$ and $We = 7 - 120$ is covered.

4. Validation

The solver FS3D is validated extensively for various applications (Kaufmann et al., 2018; Baggio and Weigand, 2019; Ren et al., 2021; Potyka et al., 2023; Palmetshofer et al., 2025). To validate the implementation with respect to wetting, several test cases as well as experimental comparisons are conducted. Static test cases include a sessile drop on a smooth surface with varying contact angles and a static meniscus in a square capillary. Droplet impacts on a smooth surface with contact angle hysteresis as well as impacts on grooves validate the solver for dynamic wetting processes. While the previous test cases were simulated using the b-CSF model, the CSS model was employed in the following simulations of a square capillary and droplet impacts on grooves, demonstrating the interchangeability of the surface tension models.

4.1. Sessile drop on a smooth surface

A simple and well-known test case is a static droplet with and without gravity. The Ohnesorge number is set to Oh ≈ 0.021 (μ = 9 mPa s, ρ = 930 kg m^{-3}, D_0 = 6 mm, σ = 30 mN m^{-1}) and the Bond number to Bo = $\rho g D_0^2/\sigma \approx 11$ such that the influence of gravity is significant. A quarter droplet is simulated in a cubic domain with two symmetry planes and a no-slip condition at the bottom whereas all other boundary conditions are a zero-gradient Neumann condition. The edge length was chosen as 5 mm and increased or decreased to 7 mm or 3 mm for the largest and smallest contact angles, respectively. For all cases a resolution of 128 grid cells in each direction was used. Thus, an equidistant resolution of $\Delta x/D_0 = 3.9\times10^{-3}, 6.5\times10^{-3}, 6.5\times10^{-3}, 6.5\times10^{-3}, 9.1\times10^{-3}$ for the cases of $\theta = 30°, 60°, 90°, 120°, 150°$ is used, respectively. The drop was initialized as a spherical cap to match the specified contact angle at the wall. The simulation was then run until a static solution was reached. A variation of the initial condition was tested and the same final solutions were obtained. Without gravity, the surface tension force at the droplet surface and the pressure jump across the interface are the only forces present and balance each other. The drop contour can then be described as a spherical cap to validate the simulation results. For comparison of the drop shapes under gravity, the shape equations derived by Bashforth and Adams (1883) were solved with an algorithm presented by Blokhuis (2003). In Fig. 9, static drop contours with and without gravity are compared with the solutions of the shape equations for various contact angles. All simulated cases match the reference solution almost exactly.

4.2. Static meniscus in a square capillary

The shape of a meniscus in a square channel in the absence of gravity can be described analytically. A similar situation can arise for the fluid flow between pillars or grooves of a structured surface after a droplet impact. The capillary pressure p_c and the meniscus height h are given as a function of the channel width a and the contact angle as (Feng and Rothstein, 2011)

$$p_c = -\frac{4\sigma\cos(\theta)}{a}, \tag{20}$$

$$h = \frac{a}{2\cos(\theta)}\left[1 - \sqrt{1 - 2\cos(\theta)^2}\right]. \tag{21}$$

The Ohnesorge number is set to Oh = $\mu/\sqrt{\rho a \sigma} \approx 0.036$ (μ = 9.15 mPa s, ρ = 930 kg m^{-3}, a = 0.9531 mm, σ = 30 mN m^{-1}). A quarter of the capillary is simulated by applying two symmetry conditions and a third one at the bottom, the other boundary conditions are set to a zero-gradient Neumann condition. The walls of the capillary are represented by a rigid body with a thickness of 0.0469 mm. The meniscus is initialized as a section of a sphere to match the contact angle at the solid interface. The simulation domain has a width and depth of 0.5 mm and a height of 1 mm and is discretized with an equidistant grid with 64 × 64 × 128 cells. Three different configurations with contact angles of $\theta = 60°, 90°, 120°$ were simulated until a static solution was reached. In this setup, the CSS model was used. In Fig. 10, the results of FS3D are compared to the analytic equations and show good agreement.

4.3. Droplet impact onto a smooth surface with contact angle hysteresis

A comparison to droplet impact experiments was performed to assess the quality of the numerical modeling for dynamic test cases. The influence of the dynamic contact angle model, especially in the receding phase, is unarguably large. In order to validate the implemented methods, it is therefore important to obtain information on the actual

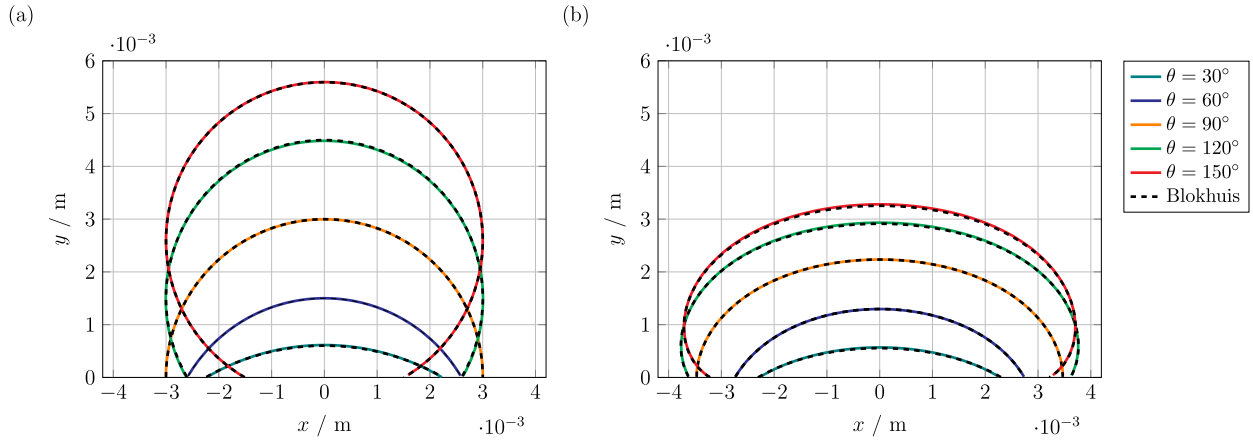

Fig. 9. Comparison of static drop contours without (a) and with (b) gravity for different contact angles.

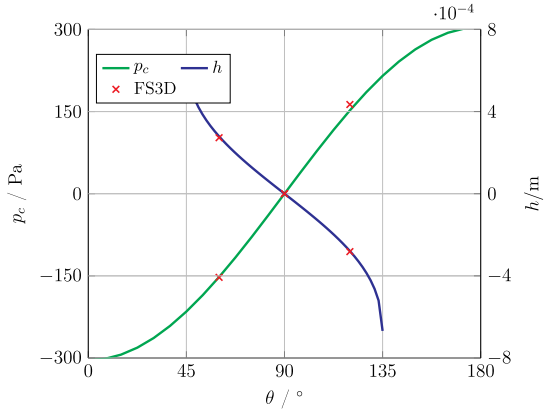

Fig. 10. Results of capillary pressure p_c and meniscus height h in a square capillary as a function of the contact angle from FS3D and the analytic solutions Eqs. (20) and (21).

contact line dynamics. Yokoi et al. (2009) investigated this influence and hence provided their fitted contact angle model as

$$\theta_{dyn}(\mathrm{Ca}) = \begin{cases} \min\left[\theta_{st} + \left(\frac{|\mathrm{Ca}|}{k_a}\right)^{\frac{1}{3}}, \theta_{adv,max}\right] & \text{if } \mathrm{Ca} \geq 0, \\ \max\left[\theta_{st} + \left(\frac{|\mathrm{Ca}|}{k_r}\right)^{\frac{1}{3}}, \theta_{rec,max}\right] & \text{if } \mathrm{Ca} < 0 \end{cases} \tag{22}$$

with the parameters $\theta_{rec,min} = 52°$ as minimal receding and $\theta_{adv,max} = 114°$ as maximal advancing contact angles as well as scaling parameters $k_r = 9.0 \cdot 10^{-8}$ and $k_a = 9.0 \cdot 10^{-9}$. Those parameters were optimized to match their experimental contact angle values for water on silane. They used the water properties $\mu = 1\,\mathrm{mPa\,s}, \rho = 1000\,\mathrm{kg\,m^{-3}}, \sigma = 72\,\mathrm{mN\,m^{-1}}$. Additionally, as described in Section 3, we conducted our own dynamic contact angle measurements for water on polycarbonate. The Hoffman graph, cf. Fig. 8, was then fitted with a linear function for the advancing and receding branch, respectively. The resulting dynamic contact angle model is shown below,

$$\theta_{dyn}(\mathrm{Ca}) = \begin{cases} 1.941 - 1.932\mathrm{Ca} & \text{if } \mathrm{Ca} \geq 0, \\ 1.179 + 311.2\mathrm{Ca} & \text{if } \mathrm{Ca} < 0. \end{cases} \tag{23}$$

For our own experiments, we determined the water properties to $\mu = 0.9700\,\mathrm{mPa\,s}$, $\rho = 997.8\,\mathrm{kg\,m^{-3}}$, $\sigma = 72.49\,\mathrm{mN\,m^{-1}}$.

For all three cases, an equidistant resolution of $\Delta x/D_0 = 3.4 \times 10^{-3}$ with an edge length of the cubic domain of 4 mm is chosen. The droplets

Table 1
Parameters of drop impacts on a smooth surface.

Case	We	Re	$\theta_{rec}, \theta_{adv}$	Substrate	Reference
1	31.67	2280	52°, 114°	silane	Yokoi et al. (2009)
2	14.06	1499	68°, 111°	polycarbonate	own
3	48.50	2757	68°, 111°	polycarbonate	own

are initialized as spheres near the wall with a thin air layer of 40 µm in between which corresponds to roughly 5 cells. The Weber number $\mathrm{We} = \rho D_0 U_0^2/\sigma$ with the initial droplet diameter D_0 and the impact speed U_0 describes the ratio of inertial and surface forces. On the other hand, the Reynolds number $\mathrm{Re} = \rho D_0 U_0/\mu$ forms the ratio of inertial to viscous forces. The spreading factor is the diameter of the wetted area relative to the initial droplet diameter $\beta = D/D_0$. Results of the spreading factors for the simulations of three cases, listed in Table 1, are compared in Fig. 11 with the experiments. The qualitative agreement is in all cases very good, especially with regard to the maximum spreading. A deviation in the final spreading is visible for case 2. Nonetheless, the implementation is considered to be correct. For case 2, Mathieu's contact angle model Eq. (15)–(17) is also employed in FS3D, applying the same static contact angles as in the linear fit Eq. for the receding and advancing branch, respectively. In the spreading phase, the difference between the fit to experimental data and Mathieu's model is negligible. During the receding phase, a much larger deviation becomes apparent. This can be clearly related to the difference in the receding branch of the Hoffman graph, cf. Fig. 8, where Mathieu's model attains much greater values than determined in the experiment. Available experimental data on the contact angle can thus improve the simulation, especially in the capillary-dominated receding phase. Note that in cases 2 and 3, the contact angle hysteresis was also accounted for. This can be seen in the constant spreading factor during maximum spreading as well as the constant graph during later phases. During these stages, the contact line is pinned and the spreading factor stays constant.

4.4. Droplet impact onto a grooved surface

As a last validation, water droplet impacts onto a grooved surface are compared to the experiment. Droplets with a Weber number of $\mathrm{We} = 14$ ($U_0 = 0.6730\,\mathrm{m\,s^{-1}}$, $D_0 = 2.225\,\mathrm{mm}$) and $\mathrm{We} = 50$ ($U_0 = 1.316\,\mathrm{m\,s^{-1}}$, $D_0 = 2.125\,\mathrm{mm}$) impacted a regularly grooved surface made of polydimethylsiloxane (PDMS) with a width, height, and spacing of $d_s = 180\,\mu\mathrm{m}$. The water properties were determined as $\mu = 1.005\,\mathrm{mPa\,s}, \rho = 998.2\,\mathrm{kg\,m^{-3}}, \sigma = 72.80\,\mathrm{mN\,m^{-1}}$.

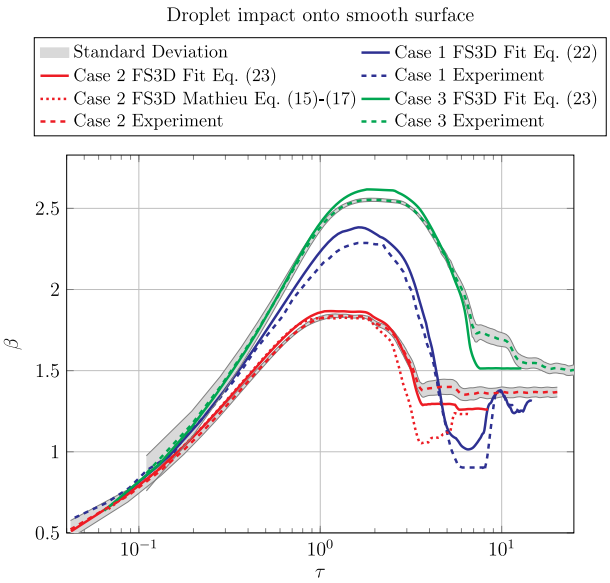

Fig. 11. Comparison of the spreading factor $\beta = \frac{D}{D_0}$ over dimensionless time $\tau = t\frac{U_0}{D_0}$ for three different cases between FS3D and experiments. Simulations with the fitted contact angle model are represented by a solid line, simulations utilizing Mathieu's model Eq. (15)–(17) by a dashed line and the standard deviation of the experiment (SD) is displayed in light gray.

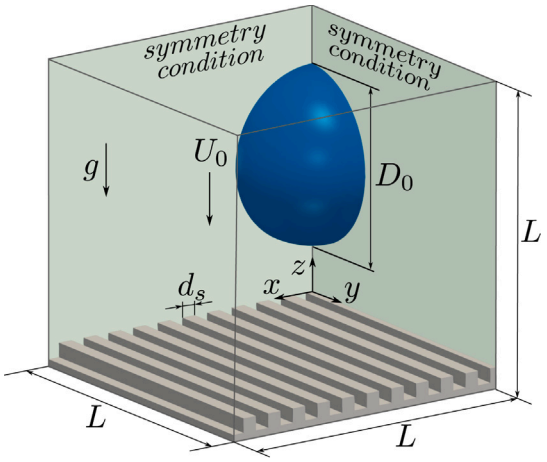

Fig. 12. Sketch of the numerical setup with coordinate system and impact parameters U_0, D_0, and d_s as well as the symmetry conditions.

Numerical setup

A sketch of the numerical setup is displayed in Fig. 12. The cubic domain with an edge length of $L = 3.84\,\text{mm}$ features two symmetry conditions, so that only a quarter of the drop is simulated. All other boundary conditions are set to a zero-gradient Neumann condition. The domain size was tested by doubling the dimensions while keeping the grid spacing constant and found to be sufficient, as this yielded the same results. The advancing and receding contact angles are set to $\theta_{adv} = 120°$ and $\theta_{rec} = 90°$, respectively, which is also reported for PDMS in the literature (Broom and Willmott, 2022; Wong et al., 2020). The CSS model is again employed for the surface tension calculation. Note that measured data for the dynamic contact angle is not available for PDMS. Mathieu's model Eq. (15)–(17) is thus chosen as the dynamic contact angle model. The impact position is set to the middle of a groove ridge. However, in the experiments, the impact location of the droplets varied between trials, which marginally influenced the overall droplet dynamics. For the validation, a trial was selected in which the droplet impacted near the center of a groove ridge. Moreover, setting the impact position in a groove valley resulted in only very slight differences in the simulation. The water droplet impact with We = 50 ($U_0 = 1.316\,\text{m s}^{-1}$, $D_0 = 2.125\,\text{mm}$) is simulated with 256, 512, and 1024 cells per domain edge length to study the grid convergence. The results for the spreading factor in transversal β_{trans} and parallel β_{para} groove direction are displayed in Fig. 13. In the parallel direction, the two higher resolutions match very well and seem to have converged. Also in the transversal direction, the graphs are very close. Since the deviation is within the range of experimental uncertainties, the resolution of 512^3 cells is selected. A groove is thus resolved by 24 cells and the droplet by approximately 280 cells per diameter.

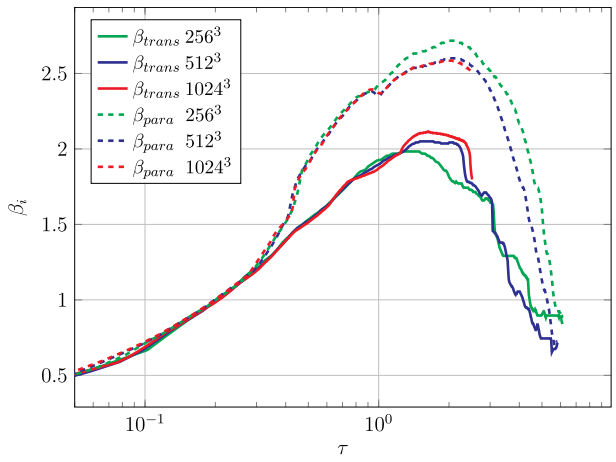

Fig. 13. Grid convergence of the spreading factor transversal to the groove direction β_{trans} and parallel β_{para} for three different resolutions.

Comparison with experiment

For the lower impact speed with We = 14, perspectives normal and parallel to the grooves are chosen. The normal perspective is a viewpoint from above in the simulation while in the experiments the images are recorded from below. A transversal as well as a parallel perspective are selected for the We = 50 impact. The comparison of simulation snapshots and experimental images is shown in Fig. 14 for the We = 14 case and in Fig. 15 for the We = 50 case.

In the normal perspective, a good qualitative agreement of interface dynamics is visible. At the timestep $\tau = 1.75$, the little cusp seen from above on the left side of the experimental image is also captured by the simulation. Also, the emerging jet in the parallel perspective is present in the numerical result. Furthermore, a timestep later, the vertical alignment of the contact line with the grooves in the normal perspective is also apparent in the simulation. For the higher impact velocity case (We = 50), the overall shapes again show a good agreement. At timestep $\tau = 2.63$, for example, in both the experiment and simulation, three distinct bulges are visible in the parallel perspective as well as only two in the transversal perspective. A quantitative comparison of the spreading factors is presented in Fig. 16. The simulation results follow the graphs of the experiments during the spreading phase well. Moreover, the maximum spreading predicted by the simulation agrees well with the experiment. Later, in the receding phase, similar to the smooth surface in Section 4.3, the results start to differ and the extend of receding is overestimated. A reasonable cause is the pinning at groove edges which slows down the retraction in the experiments. This effect is not considered in the simulations so far as it would require special treatment, see Section 2.2.2. Additionally, it is likely that the dynamic receding contact angle exhibits rather low values similar to the smooth surface (cf. Fig. 8), which is not captured by Mathieu's model.

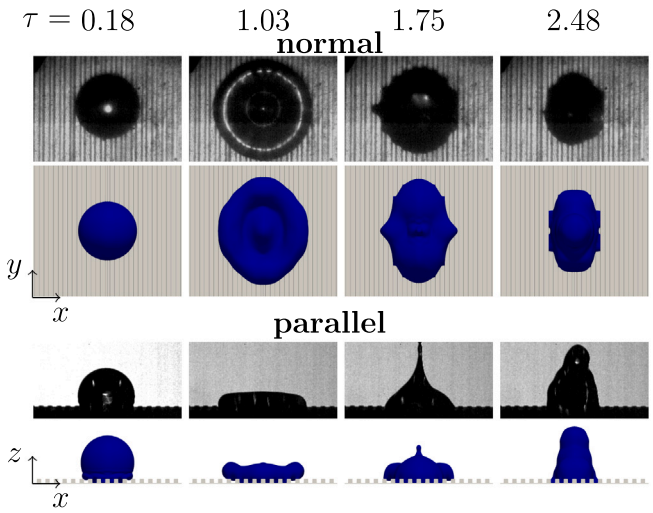

Fig. 14. Simulation snapshots and experimental images of a droplet impact with We = 14 onto a grooved surface from different perspectives and time steps. The experimental images are contrast-adjusted for better visibility.

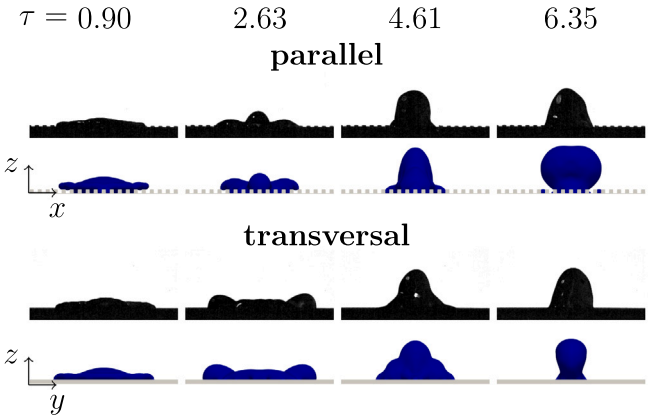

Fig. 15. Simulation snapshots and experimental images of a droplet impact with We = 50 onto a grooved surface from different perspectives and time steps.

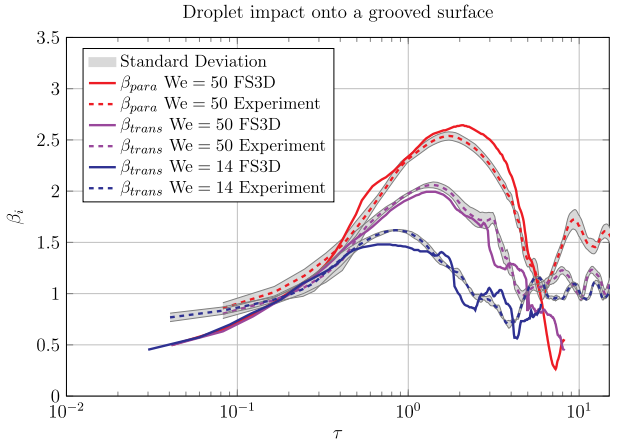

Fig. 16. Comparison of spreading factors as function of the dimensionless time $\tau = t\frac{U_0}{D_0}$ between FS3D and experiments.

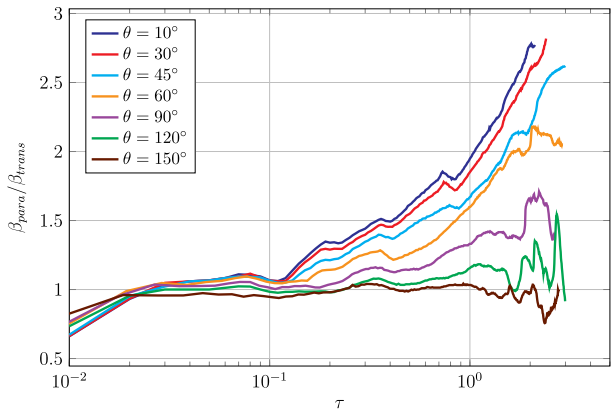

Fig. 17. Comparison of the anisotropy for a droplet impact onto grooves as function of the dimensionless time $\tau = t\frac{U_0}{D_0}$ between different contact angles.

5. Results and discussion

As described in Section 1, most studies about droplet impact onto a grooved surface focused on one or two different solid materials and were mostly hydrophobic. We therefore explore in this chapter the influence of the wettability by varying the contact angle from hydrophilic to hydrophobic. The contact angle was varied from $\theta = 10°$ to $\theta = 150°$ while keeping the Weber number and groove geometry constant. These parameters are set as in the validation case (Section 4.4) with We = 14, $d_s = 180\,\mu m$ and the same water properties are used. Again, the spreading is quantified by the spreading factor in parallel and transversal direction to the grooves with $\beta_{para} = \frac{D_{para}}{D_0}$ and $\beta_{trans} = \frac{D_{trans}}{D_0}$. Mathieu's contact angle model is employed without a hysteresis interval because the wettabilities considered are purely hypothetical. Furthermore, choosing the fitted model from would restrict the range of variation as the limits of 0° and 180° are quickly reached.

Due to the unidirectional surface structure of grooves, the spreading is in general more pronounced in the parallel direction of the grooves. When increasing the wettability (lowering the contact angle), we noticed a further increase in anisotropy. This can be expressed by the ratio of the parallel and transversal spreading factor $\beta_{para}/\beta_{trans}$, where a value of one means perfect symmetry. Fig. 17 compares this ratio during spreading for seven different contact angles. At $\theta = 120°$ and above, the anisotropy stays very close to unity during the process. This can also be clearly seen in Fig. 18 for $\tau = 0.7$ and $\tau = 2$ where these two cases show an almost circular shape in a perspective from above. An explanation can be found in the parallel perspective. The droplet of the 120°-case penetrates only into four grooves at $\tau = 0.7$, cf. Fig. 19, and later at $\tau = 2$ reduces this count to two, caused by the high capillary pressure needed to penetrate a groove. The droplet with the lowest wettability (highest contact angle) only begins to penetrate two grooves at $\tau = 0.7$ but does not wet the bottom of a groove. Those impacts are thus hardly affected by the groove structure and remain symmetric. A slight rise and later decline of the directional dependence is visible for $\theta = 90°$, which can be seen as an intermediate case where no pressure difference is needed to penetrate the grooves. From $\theta = 60°$ and below, the propagation apparently occurs strongly along the grooves, as the ratio of spreading factors is much higher compared to the other cases. When examining again Fig. 18, it becomes clear that after an initial spreading also transversal to the grooves, the droplets mainly continue to spread parallel to the grooves.

This can be further seen by comparing Fig. 20 for the transversal and Fig. 21 for the parallel spreading factor. Surprisingly, the transversal spreading is mostly independent of the wettability and is thus governed by inertia and the obstruction of the grooves. Only for the very low contact angles of $\theta = 45°$ and lower, the droplet is able to cross another

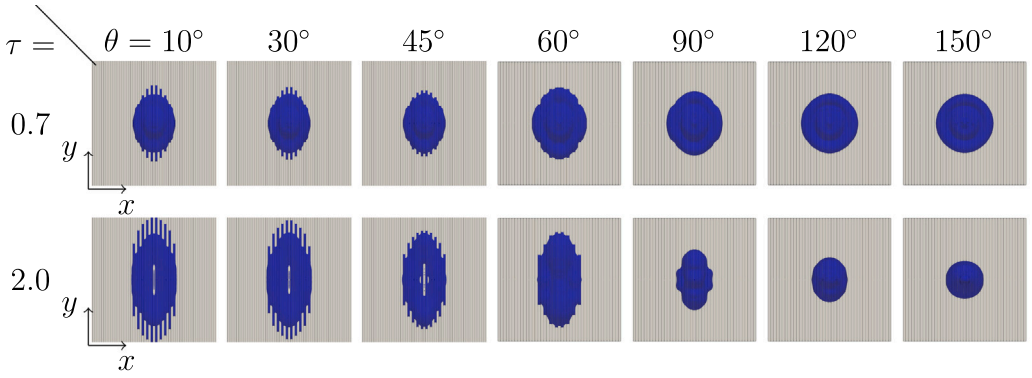

Fig. 18. Simulation snapshots of a droplet impact onto grooves at different time steps τ from an above viewpoint for different contact angles.

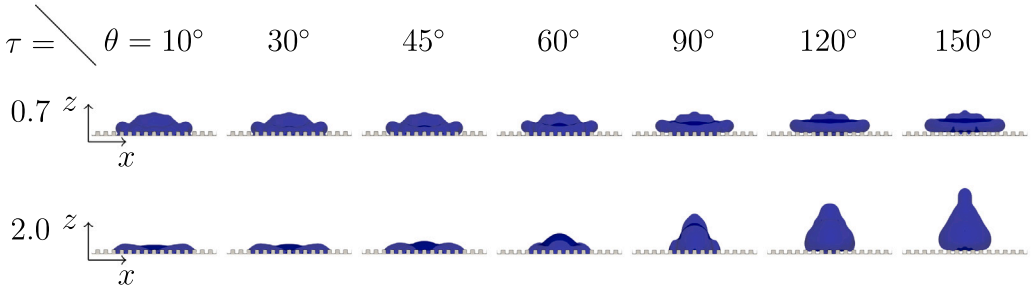

Fig. 19. Simulation snapshots of a droplet impact onto grooves at different time steps τ from a parallel perspective for different contact angles.

groove due to the capillary force pulling outwards. The spreading parallel to the grooves behaves similarly as it would be expected on a smooth surface, which was also observed by Vaikuntanathan and Sivakumar (2016), and shows a clear dependence on the wettability. Above $\theta = 90°$ and from $\theta = 45°$ and below, a further change of the contact angle seems to influence the spreading only slightly. For the high contact angles, the reason is still the weak penetration of the grooves as explained above. Considering the three lowest contact angles, the spreading can be explained with the theory of the meniscus shape in a square capillary. For an n-sided regular polygonal capillary without gravity, the critical contact angle (Feng and Rothstein, 2011) is $\theta_c = \pi/n$ and hence for a square capillary $\theta_{c,sq} = 45°$. From this critical angle and below, no stable meniscus can form in the corners of the capillary and so called corner flow forms and pulls the liquid upwards in the capillary. As the groove size is well below the capillary length of water, $d_s = 0.18\,\text{mm} < l_c = \sqrt{\sigma/(\rho g)} \approx 2.7\,\text{mm}$, the effect of gravity can be neglected inside the grooves. Thus, the shape of the interface after the inertial spreading is close to the theoretic shape in a square capillary especially near the corners. This explains the continued spreading for the cases of $\theta = 45°$ and below, where the capillary forces are pulling the liquid outwards.

Malla et al. (2017) investigated experimentally how this anisotropic behavior changes with respect to the Weber number, using grooves with a height and width of 27 µm and 22 µm, respectively, and a pitch in the range of 30 µm to 76 µm. They reported a decrease in anisotropy with increasing Weber numbers and reasoned with the different energy contributions. According to them, a significant share of the surface energy is coming from contact line pinning at the groove edges but is dominated at higher impact speeds by the kinetic energy. Thus, the anisotropy would decrease at higher Weber numbers. Vaikuntanathan and Sivakumar (2016), on the other hand, observed the opposite in their experiments with groove sizes in the range of $d_s = 125\,\mu\text{m}$ to $180\,\mu\text{m}$. This was also attributed to contact line pinning at the groove edges. They argued that as spreading generally increases with higher Weber numbers, the number of grooves that the droplet must cross also increases and therefore the resistance in transversal

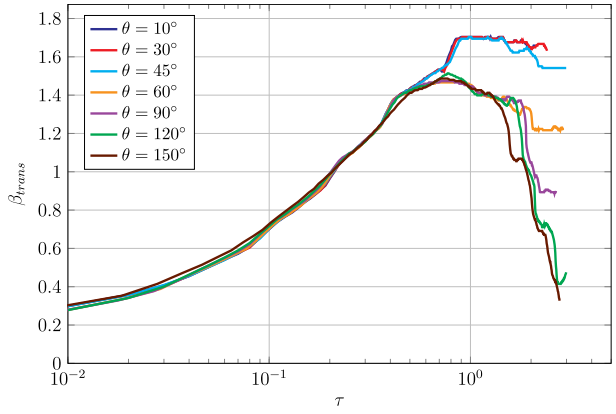

Fig. 20. Comparison of transversal spreading factors for a droplet impact onto grooves as function of the dimensionless time $\tau = t\frac{U_0}{D_0}$ between different contact angles.

spreading. This consequently would lead to an increase in anisotropy at higher Weber numbers.

We attempted to clarify this difference and conducted a parameter study on the Weber number for our setup. A groove size of 180 µm is again employed with a contact angle of $\theta = 90°$ to be close to the experiments. The Weber number was varied from We = 2 to We = 62 and the maximum spreading factor in parallel and transversal direction was evaluated. The results are summarized in Fig. 22. The maximum parallel as well as transversal spreading factors increase consistently with the Weber number. This is additionally reflected in the anisotropy expressed as the ratio $\beta_{para}^{max}/\beta_{trans}^{max}$. With the exception of a slight decrease at We = 6, the anisotropy also increases. One reason for this could be the low impact speeds, which limits the number of grooves crossed during spreading. Specifically for We = 6, the droplet spreads just reaching another groove edge and continues to spread

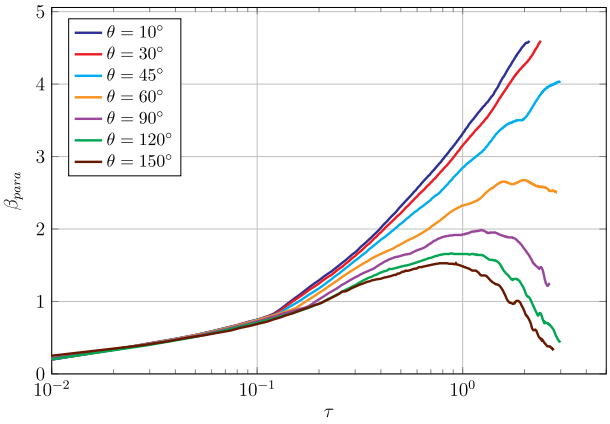

Fig. 21. Comparison of parallel spreading factors for a droplet impact onto grooves as function of the dimensionless time $\tau = t\frac{U_0}{D_0}$ between different contact angles.

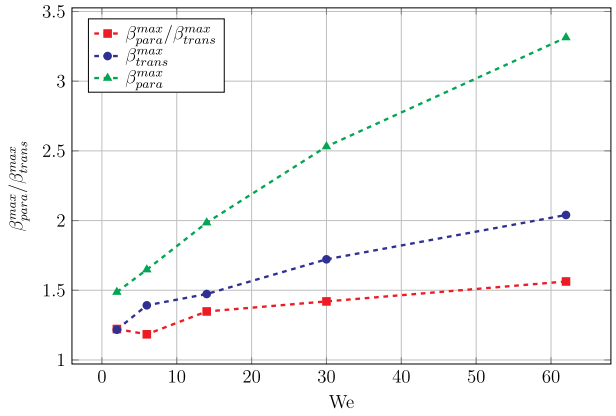

Fig. 22. Dependence of the maximum spreading factor and anisotropy on the Weber number for a droplet impact onto grooves with $\theta = 90°$.

due to wettability, which is also visible in the transversal spreading factor. The same effect can be seen in Fig. 20 for contact angles $\theta = 45°$ and below, where the droplets also reach another groove edge, resulting in a pronounced spreading factor. Nonetheless, we conclude that for droplet impacts onto grooves of sizes similar to 180 µm, the anisotropy increases with the Weber number. Therefore, the result is consistent with the findings of Vaikuntanathan and Sivakumar (2016), although the range of groove sizes investigated by Malla et al. (2017) is significantly smaller and our results are thus not fully transferable.

6. Conclusion

In this study, a robust Volume-of-Fluid framework was developed and validated within the incompressible multiphase flow solver FS3D to investigate the influence of wettability on droplet impact onto grooved surfaces, with a particular focus on relatively unexplored hydrophilic cases. The developed framework benefits from the integration of a PLIC scheme for the interface reconstruction at the wall (Potyka and Schulte, 2024) and uses Sussman's method (Sussman, 2001) for contact line modeling. It is compatible with both the Balanced Continuum Surface Force (b-CSF) (Popinet, 2009) and Continuum Surface Stress (Lafaurie et al., 1994) surface tension models. A mesh-dependent dynamic contact angle model based on Cox's theory (Afkhami et al., 2009) was also implemented. This model significantly improves grid convergence properties by counteracting numerical slip, which is a common challenge in simulations of moving contact lines. This unique combination of methods enables robust descriptions of contact line dynamics in a wide range of applications, from capillary-driven cases to situations involving complex topological changes on smooth and structured surfaces.

Validation against analytical solutions for static cases and new experimental data for droplet impacts on smooth and grooved surfaces showed excellent agreement in spreading dynamics, particularly the maximum spreading factor. Discrepancies in the receding phase could be attributed to the limitations of dynamic contact angle models in accurately capturing receding behavior, particularly in the presence of contact angle hysteresis or pinning effects at groove edges. This highlights the importance of precise experimental data on dynamic contact angles to enhance the predictive capabilities of capillary-dominated phases.

The goal of our study was to fill the gap in understanding the impact of wettability on spreading on grooved surfaces. A comprehensive parameter study revealed an increase of anisotropy with wettability. While spreading transverse to the grooves was found to be largely independent of wettability, being primarily governed by inertia and the physical obstruction of the grooves, spreading parallel to the grooves depended strongly on wettability, behaving similarly to spreading on a smooth substrate. For contact angles $\leq 45°$, corner flow was the dominant spreading mechanism within grooves, consistent with theoretical predictions. Highly hydrophobic surfaces ($\geq 120°$) showed minimal groove interaction and nearly isotropic spreading due to insufficient penetration into the groove structures.

In summary, this work provides a validated novel numerical framework for studying the impact of droplets on structured surfaces, offering new insights into the interplay between wettability, surface structures and dynamic wetting phenomena. These findings deepen our understanding of anisotropic spreading and the role of corner flow in hydrophilic conditions, which is essential for the rational design and optimization of advanced materials for applications such as microfluidics, surface coatings and thermal management.

CRediT authorship contribution statement

Jonathan Wurst: Writing – review & editing, Writing – original draft, Visualization, Validation, Software, Methodology, Investigation, Formal analysis, Data curation, Conceptualization. **Maximilian Dreisbach:** Writing – review & editing, Writing – original draft, Visualization, Validation, Methodology, Investigation, Data curation. **Alexander Stroh:** Writing – review & editing, Supervision, Resources, Project administration, Methodology, Funding acquisition, Conceptualization. **Jochen Kriegseis:** Writing – review & editing, Supervision, Resources, Project administration, Methodology, Funding acquisition, Conceptualization. **Kathrin Schulte:** Writing – review & editing, Supervision, Resources, Project administration, Methodology, Funding acquisition, Formal analysis, Conceptualization.

Declaration of competing interest

The authors declare that they have no known competing financial interests or personal relationships that could have appeared to influence the work reported in this paper.

Acknowledgments

We appreciate the financial support of this work by the Friedrich and Elisabeth Boysen Foundation under grant "BOY-160". In addition, we kindly acknowledge funding by the Deutsche Forschungsgemeinschaft (DFG), Germany under Germany's Excellence Strategy - EXC 2075 - 39074001. Lastly, we would like to thank the High-Performance Computing Center Stuttgart (HLRS) for providing computation time on the HPE Apollo (Hawk) and HPE Cray EX4000 (Hunter) platforms under grant number FS3D/11142.

Data availability

The data that support the findings of this study are openly available in DaRUS at https://doi.org/10.18419/DARUS-5496:

Replication Data for: PLIC-based contact line modeling for simulations of droplet impact onto smooth and structured surfaces (Original data) (DaRUS)

References

Afkhami, S., Bussmann, M., 2008. Height functions for applying contact angles to 3D VOF simulations. Internat. J. Numer. Methods Fluids 61 (8), 827–847. http://dx.doi.org/10.1002/fld.1974.

Afkhami, S., Zaleski, S., Bussmann, M., 2009. A mesh-dependent model for applying dynamic contact angles to VOF simulations. J. Comput. Phys. 228 (15), 5370–5389. http://dx.doi.org/10.1016/j.jcp.2009.04.027.

Albert, C., Raach, H., Bothe, D., 2012. Influence of surface tension models on the hydrodynamics of wavy laminar falling films in volume of fluid-simulations. Int. J. Multiph. Flow 43, 66–71. http://dx.doi.org/10.1016/j.ijmultiphaseflow.2012.02.011.

Baggio, M., Weigand, B., 2019. Numerical simulation of a drop impact on a superhydrophobic surface with a wire. Phys. Fluids 31 (11), http://dx.doi.org/10.1063/1.5123593.

Bashforth, F., Adams, J.C., 1883. An Attempt to Test the Theories of Capillary Action. Cambridge University Press.

Blokhuis, E.M., 2003. Surface and interfacial tension: Measurement, theory, and applications. pp. 149–164. http://dx.doi.org/10.1201/9780203021262.

Brackbill, J.U., Kothe, D.B., Zemach, C., 1992. A continuum method for modeling surface-tension. J. Comput. Phys. 100 (2), 335–354. http://dx.doi.org/10.1016/0021-9991(92)90240-Y.

Broom, M., Willmott, G.R., 2022. Water drop impacts on regular micropillar arrays: The impact region. Phys. Fluids 34 (1), http://dx.doi.org/10.1063/5.0078792.

Chen, X., Han, T., Pan, J., Fuster, D., Zaleski, S., 2025. Volume-conserving method for dynamic contact line on complex surfaces. Phys. Fluids 37 (2), http://dx.doi.org/10.1063/5.0254089.

Clanet, C., Béguin, C., Richard, D., Quéré, D., 2004. Maximal deformation of an impacting drop. J. Fluid Mech. 517, 199–208. http://dx.doi.org/10.1017/s0022112004000904.

Cossali, G.E., Coghe, A., Marengo, M., 1997. The impact of a single drop on a wetted solid surface. Exp. Fluids 22 (6), 463–472. http://dx.doi.org/10.1007/s003480050073.

Cox, R.G., 1986. The dynamics of the spreading of liquids on a solid surface. Part 1. Viscous flow. J. Fluid Mech. 168 (1), 169. http://dx.doi.org/10.1017/s0022112086000332.

Das, S., Patel, H.V., Milacic, E., Deen, N.G., Kuipers, J.A.M., 2018. Droplet spreading and capillary imbibition in a porous medium: A coupled IB-VOF method based numerical study. Phys. Fluids 30 (1), http://dx.doi.org/10.1063/1.5010716.

Deng, W., Gomez, A., 2011. Electrospray cooling for microelectronics. Int. J. Heat Mass Transfer 54 (11–12), 2270–2275. http://dx.doi.org/10.1016/j.ijheatmasstransfer.2011.02.038.

Dreisbach, M., 2025. Spatio-Temporal Interface Reconstruction by Means of Glare Points and Deep Learning (Ph.D. thesis). Karlsruher Institut für Technologie (KIT), http://dx.doi.org/10.5445/IR/1000180490.

Dreisbach, M., Blessing, S., Brunn, A., Michaux, F., Stroh, A., Kriegseis, J., 2023. Three-dimensional encoding of a gas–liquid interface by means of color-coded glare points. Exp. Fluids 64 (3), http://dx.doi.org/10.1007/s00348-023-03592-0.

Dupont, J.-B., Legendre, D., 2010. Numerical simulation of static and sliding drop with contact angle hysteresis. J. Comput. Phys. 229 (7), 2453–2478. http://dx.doi.org/10.1016/j.jcp.2009.07.034.

Eggers, J., Fontelos, M.A., Josserand, C., Zaleski, S., 2010. Drop dynamics after impact on a solid wall: Theory and simulations. Phys. Fluids 22 (6), http://dx.doi.org/10.1063/1.3432498.

Eisenschmidt, K., Ertl, M., Gomaa, H., Kieffer-Roth, C., Meister, C., Rauschenberger, P., Reitzle, M., Schlottke, K., Weigand, B., 2016. Direct numerical simulations for multiphase flows: An overview of the multiphase code FS3D. J. Appl. Math. Comput. 272 (2), 508–517. http://dx.doi.org/10.1016/j.amc.2015.05.095.

Feng, J., Rothstein, J.P., 2011. Simulations of novel nanostructures formed by capillary effects in lithography. J. Colloid Interface Sci. 354 (1), 386–395. http://dx.doi.org/10.1016/j.jcis.2010.10.030.

Fink, V., Cai, X., Stroh, A., Bernard, R., Kriegseis, J., Frohnapfel, B., Marschall, H., Wörner, M., 2018. Drop bouncing by micro-grooves. Int. J. Heat Fluid Flow 70, 271–278. http://dx.doi.org/10.1016/j.ijheatfluidflow.2018.02.014.

Foltyn, P., Ribeiro, D., Silva, A., Lamanna, G., Weigand, B., 2022. Influence of wetting behavior on the morphology of droplet impacts onto dry-patterned micro-structured surfaces. Phys. Fluids 34 (12), 123322. http://dx.doi.org/10.1063/5.0124692.

Göhl, J., Mark, A., Sasic, S., Edelvik, F., 2018. An immersed boundary based dynamic contact angle framework for handling complex surfaces of mixed wettabilities. Int. J. Multiph. Flow 109, 164–177. http://dx.doi.org/10.1016/j.ijmultiphaseflow.2018.08.001.

Gründing, D., Smuda, M., Antritter, T., Fricke, M., Rettenmaier, D., Kummer, F., Stephan, P., Marschall, H., Bothe, D., 2020. A comparative study of transient capillary rise using direct numerical simulations. Appl. Math. Model. 86, 142–165. http://dx.doi.org/10.1016/j.apm.2020.04.020.

Guo, C., Zhao, D., Sun, Y., Wang, M., Liu, Y., 2018. Droplet impact on anisotropic superhydrophobic surfaces. Langmuir 34 (11), 3533–3540. http://dx.doi.org/10.1021/acs.langmuir.7b03752.

Harlow, F.H., Welch, J.E., 1965. Numerical calculation of time-dependent viscous incompressible flow of fluid with free surface. Phys. Fluids 8 (12), 2182–2189.

Hirt, C.W., Nichols, B.D., 1981. Volume of fluid (VOF) method for the dynamics of free boundaries. J. Comput. Phys. 39 (1), 201–225. http://dx.doi.org/10.1016/0021-9991(81)90145-5.

Hu, Z., Chu, F., Wu, X., 2022. Design principle of ridge-textured superhydrophobic surfaces for inducing pancake bouncing. Int. Commun. Heat Mass Transfer 136, 106167. http://dx.doi.org/10.1016/j.icheatmasstransfer.2022.106167.

Huang, R., Gong, J., Jiang, Z., Zhang, N., Hou, J., 2025. Numerical simulation study of droplet impact on microscale groove-textured superhydrophobic surface: Influence of geometric structural parameters. Colloids Surfaces A: Physicochem. Eng. Asp. 709, 136053. http://dx.doi.org/10.1016/j.colsurfa.2024.136053.

Huh, C., Scriven, L., 1971. Hydrodynamic model of steady movement of a solid/liquid/fluid contact line. J. Colloid Interface Sci. 35 (1), 85–101. http://dx.doi.org/10.1016/0021-9797(71)90188-3.

Jansen, H.P., Sotthewes, K., Ganser, C., Teichert, C., Zandvliet, H.J.W., Kooij, E.S., 2012. Tuning kinetics to control droplet shapes on chemically striped patterned surfaces. Langmuir 28 (37), 13137–13142. http://dx.doi.org/10.1021/la302551m.

Jin, L., Wang, Y., 2020. Droplet impact on groove-patterned surfaces: The role of the groove patterns and impact velocities. Colloid Interface Sci. Commun. 37, 100287. http://dx.doi.org/10.1016/j.colcom.2020.100287.

Kannan, R., Sivakumar, D., 2008. Drop impact process on a hydrophobic grooved surface. Colloids Surfaces A: Physicochem. Eng. Asp. 317 (1–3), 694–704. http://dx.doi.org/10.1016/j.colsurfa.2007.12.005.

Kaufmann, J., Geppert, A., Ertl, M., Bernard, R., Vaikuntanathan, V., Lamanna, G., Weigand, B., 2018. Direct numerical simulations of one-and two-component droplet wall-film interactions within the crown-type splashing regime. In: ICLASS 2018, 14th Triennial International Conference on Liquid Atomization and Spray Systems.

Kistler, S.F., 1993. Wettability. CRC Press, http://dx.doi.org/10.1201/9781482277500,

Lafaurie, B., Nardone, C., Scardovelli, R., Zaleski, S., Zanetti, G., 1994. Modelling merging and fragmentation in multiphase flows with SURFER. J. Comput. Phys. 113 (1), 134–147. http://dx.doi.org/10.1006/jcph.1994.1123.

Legendre, D., Maglio, M., 2013. Numerical simulation of spreading drops. Colloids Surfaces A: Physicochem. Eng. Asp. 432, 29–37. http://dx.doi.org/10.1016/j.colsurfa.2013.04.046.

Léopoldès, J., Dupuis, A., Bucknall, D.G., Yeomans, J.M., 2003. Jetting micron-scale droplets onto chemically heterogeneous surfaces. Langmuir 19 (23), 9818–9822. http://dx.doi.org/10.1021/la0353069.

Lin, D.-J., Wang, L., Wang, X.-D., Yan, W.-M., 2019. Reduction in the contact time of impacting droplets by decorating a rectangular ridge on superhydrophobic surfaces. Int. J. Heat Mass Transfer 132, 1105–1115. http://dx.doi.org/10.1016/j.ijheatmasstransfer.2018.12.087.

Linder, N., Criscione, A., Roisman, I.V., Marschall, H., Tropea, C., 2015. 3D computation of an incipient motion of a sessile drop on a rigid surface with contact angle hysteresis. Theor. Comput. Fluid Dyn. 29 (5–6), 373–390. http://dx.doi.org/10.1007/s00162-015-0362-9.

Liu, Y., Moevius, L., Xu, X., Qian, T., Yeomans, J.M., Wang, Z., 2014. Pancake bouncing on superhydrophobic surfaces. Nat. Phys. 10 (7), 515–519. http://dx.doi.org/10.1038/nphys2980.

Malla, L.K., Patil, N.D., Bhardwaj, R., Neild, A., 2017. Droplet bouncing and breakup during impact on a microgrooved surface. Langmuir 33 (38), 9620–9631. http://dx.doi.org/10.1021/acs.langmuir.7b02183.

Mao, T., Kuhn, D.C.S., Tran, H., 1997. Spread and rebound of liquid droplets upon impact on flat surfaces. AIChE J. 43 (9), 2169–2179. http://dx.doi.org/10.1002/aic.690430903.

Marmur, A., Della Volpe, C., Siboni, S., Amirfazli, A., Drelich, J.W., 2017. Contact angles and wettability: towards common and accurate terminology. Surf. Innov. 5 (1), 3–8. http://dx.doi.org/10.1680/jsuin.17.00002.

Mathieu, B., 2003. Etudes physique, expérimentale et numérique des mécanismes de base intervenant dans les écoulements diphasiques en micro-fluidique (Ph.D. thesis). Université de Provence.

Milacic, E., Baltussen, M., Kuipers, J., 2019. Direct numerical simulation study of droplet spreading on spherical particles. Powder Technol. 354, 11–18. http://dx.doi.org/10.1016/j.powtec.2019.05.064.

Mundo, C., Sommerfeld, M., Tropea, C., 1995. Droplet-wall collisions - Experimental studies of the deformation and breakup process. Int. J. Multiph. Flow 21 (2), 151–173. http://dx.doi.org/10.1016/0301-9322(94)00069-V.

Neinhuis, C., 1997. Characterization and distribution of water-repellent, self-cleaning plant surfaces. Ann. Botany 79 (6), 667–677. http://dx.doi.org/10.1006/anbo.1997.0400.

Palmetshofer, P., Hengsbach, S., Guttmann, M., Worgull, M., Weigand, B., 2024. Azimuthal variation of apparent contact angles on structured surfaces featuring micrometric ramps, pyramids and staggered cubes at two different inherent wettabilities. http://dx.doi.org/10.48550/ARXIV.2411.06961.

Palmetshofer, P., Wurst, J., Geppert, A.K., Schulte, K., Cossali, G.E., Weigand, B., 2025. Wetting behavior in the inertial phase of droplet impacts onto sub-millimeter microstructured surfaces. J. Colloid Interface Sci. 682, 413–422. http://dx.doi.org/10.1016/j.jcis.2024.11.154.

PasandidehFard, M., Qiao, Y.M., Chandra, S., Mostaghimi, J., 1996. Capillary effects during droplet impact on a solid surface. Phys. Fluids 8 (3), 650–659. http://dx.doi.org/10.1063/1.868850.

Patankar, N.A., Singh, P., Joseph, D.D., Glowinski, R., Pan, T.-W., 2000. A new formulation of the distributed Lagrange multiplier/fictitious domain method for particulate flows. Int. J. Multiph. Flow 26, 1509–1524. http://dx.doi.org/10.1016/S0301-9322(99)00100-7.

Patel, H., Das, S., Kuipers, J., Padding, J., Peters, E., 2017. A coupled Volume of Fluid and Immersed Boundary Method for simulating 3D multiphase flows with contact line dynamics in complex geometries. Chem. Eng. Sci. 166, 28–41. http://dx.doi.org/10.1016/j.ces.2017.03.012.

Pathak, A., Raessi, M., 2016a. A 3D, fully Eulerian, VOF-based solver to study the interaction between two fluids and moving rigid bodies using the fictitious domain method. J. Comput. Phys. 311, 87–113. http://dx.doi.org/10.1016/j.jcp.2016.01.025.

Pathak, A., Raessi, M., 2016b. A three-dimensional volume-of-fluid method for reconstructing and advecting three-material interfaces forming contact lines. J. Comput. Phys. 307, 550–573. http://dx.doi.org/10.1016/j.jcp.2015.11.062.

Popinet, S., 2009. An accurate adaptive solver for surface-tension-driven interfacial flows. J. Comput. Phys. 228 (16), 5838–5866. http://dx.doi.org/10.1016/j.jcp.2009.04.042.

Potyka, J., Schulte, K., 2024. A volume of fluid method for three dimensional direct numerical simulations of immiscible droplet collisions. Int. J. Multiph. Flow 170, 104654. http://dx.doi.org/10.1016/j.ijmultiphaseflow.2023.104654.

Potyka, J., Schulte, K., Planchette, C., 2023. Liquid distribution after head-on separation of two colliding immiscible liquid droplets. Phys. Fluids 35 (10), http://dx.doi.org/10.1063/5.0168080.

Range, K., Feuillebois, F., 1998. Influence of surface roughness on liquid drop impact. J. Colloid Interface Sci. 203 (1), 16–30. http://dx.doi.org/10.1006/jcis.1998.5518.

Rauschenberger, P., Weigand, B., 2015. Direct numerical simulation of rigid bodies in multiphase flow within an Eulerian framework. J. Comput. Phys. 291, 238–253. http://dx.doi.org/10.1016/j.jcp.2015.03.023.

Ren, W., Foltyn, P., Geppert, A., Weigand, B., 2021. Air entrapment and bubble formation during droplet impact onto a single cubic pillar. Sci. Rep. 11 (1), http://dx.doi.org/10.1038/s41598-021-97376-3.

Renardy, Y., Renardy, M., 2002. PROST: A parabolic reconstruction of surface tension for the volume-of-fluid method. J. Comput. Phys. 183 (2), 400–421.

Renardy, M., Renardy, Y., Li, J., 2001. Numerical simulation of moving contact line problems using a volume-of-fluid method. J. Comput. Phys. 171 (1), 243–263. http://dx.doi.org/10.1006/jcph.2001.6785.

Rider, W.J., Kothe, D.B., 1998. Reconstructing volume tracking. J. Comput. Phys. 141 (2), 112–152. http://dx.doi.org/10.1006/jcph.1998.5906.

Rieber, M., 2004. Numerische Modellierung der Dynamik freier Grenzflächen in Zweiphasenströmungen (Ph.D. thesis). Universität Stuttgart.

Roisman, I.V., 2009. Inertia dominated drop collisions. II. An analytical solution of the Navier–Stokes equations for a spreading viscous film. Phys. Fluids 21 (5), http://dx.doi.org/10.1063/1.3129283.

Scheller, B.L., Bousfield, D.W., 1995. Newtonian drop impact with a solid surface. AIChE J. 41 (6), 1357–1367. http://dx.doi.org/10.1002/aic.690410602.

Settles, G.S., 2001. Schlieren and Shadowgraph Techniques. Springer Berlin Heidelberg.

Steigerwald, J., Ibach, M., Geppert, A.K., Weigand, B., 2024. Numerical investigation of drop–film interactions with a thixotropic liquid. J. Non-Newton. Fluid Mech. 329, 105259. http://dx.doi.org/10.1016/j.jnnfm.2024.105259.

Stow, C.D., Hadfield, M.G., 1981. Proc. R. Soc. A 373 (1755), 419–441. http://dx.doi.org/10.1098/rspa.1981.0002.

Strang, G., 1968. On the construction and comparison of difference schemes. SIAM J. Numer. Anal. 5 (3), 506–517. http://dx.doi.org/10.1137/0705041.

Sun, X., Sakai, M., 2015. Three-dimensional simulation of gas–solid–liquid flows using the DEM–VOF method. Chem. Eng. Sci. 134, 531–548. http://dx.doi.org/10.1016/j.ces.2015.05.059.

Sun, X., Sakai, M., 2016. Numerical simulation of two-phase flows in complex geometries by using the volume-of-fluid/immersed-boundary method. Chem. Eng. Sci. 139, 221–240. http://dx.doi.org/10.1016/j.ces.2015.09.031.

Sussman, M., 2001. An Adaptive Mesh Algorithm for Free Surface Flows in General Geometries. Chapman and Hall/CRC Boca Raton, FL, USA, pp. 207–231.

Tavares, M., Josserand, C., Limare, A., Lopez-Herrera, J.M., Popinet, S., 2024. A coupled VOF/embedded boundary method to model two-phase flows on arbitrary solid surfaces. Comput. & Fluids 278, 106317. http://dx.doi.org/10.1016/j.compfluid.2024.106317.

Tryggvason, G., Scardovelli, R., Zaleski, S., 2011. Direct Numerical Simulations of Gas–Liquid Multiphase Flows. Cambridge University Press.

Tümer, E.H., Erbil, H.Y., Akdoğan, N., 2022. Wetting of superhydrophobic polylactic acid micropillared patterns. Langmuir 38 (32), 10052–10064. http://dx.doi.org/10.1021/acs.langmuir.2c01708.

Ukiwe, C., Kwok, D.Y., 2004. On the maximum spreading diameter of impacting droplets on well-prepared solid surfaces. Langmuir 21 (2), 666–673. http://dx.doi.org/10.1021/la0481288.

Vaikuntanathan, V., Sivakumar, D., 2016. Maximum spreading of liquid drops impacting on groove-textured surfaces: Effect of surface texture. Langmuir 32 (10), 2399–2409. http://dx.doi.org/10.1021/acs.langmuir.5b04639.

van Leer, B., 1979. Towards the ultimate conservative difference scheme. V. A second-order sequel to Godunov's method. J. Comput. Phys. 32 (1), 101–136. http://dx.doi.org/10.1016/0021-9991(79)90145-1.

Wang, Y., Shangguan, Q., Zhang, D., 2019. Many-body dissipative particle dynamics simulation of the anisotropic effect of droplet wetting on stripe-patterned heterogeneous surfaces. Appl. Surf. Sci. 494, 675–683. http://dx.doi.org/10.1016/j.apsusc.2019.07.213.

Wesseling, P., 1992. An Introduction to Multigrid Methods. John Wiley & Sons.

Wong, W.S.Y., Hauer, L., Naga, A., Kaltbeitzel, A., Baumli, P., Berger, R., D'Acunzi, M., Vollmer, D., Butt, H.-J., 2020. Adaptive wetting of polydimethylsiloxane. Langmuir 36 (26), 7236–7245. http://dx.doi.org/10.1021/acs.langmuir.0c00538.

Worthington, A.M., 1876. On the forms assumed by drops of liquids falling vertically on a horizontal plate. Proc. R. Soc. Lond. 25 (171–178), 261–272. http://dx.doi.org/10.1098/rspl.1876.0048.

Yokoi, K., 2013. A practical numerical framework for free surface flows based on CLSVOF method, multi-moment methods and density-scaled CSF model: Numerical simulations of droplet splashing. J. Comput. Phys. 232 (1), 252–271. http://dx.doi.org/10.1016/j.jcp.2012.08.034.

Yokoi, K., Vadillo, D., Hinch, J., Hutchings, I., 2009. Numerical studies of the influence of the dynamic contact angle on a droplet impacting on a dry surface. Phys. Fluids 21 (7), http://dx.doi.org/10.1063/1.3158468.

Young, T., 1805. An essay on the cohesion of fluids. Philos. Trans. R. Soc. Lond. 95, 65–87. http://dx.doi.org/10.1098/rstl.1805.0005.

Youngs, D., 1984. An Interface Tracking Method for a 3d Eulerian Hydrodynamics Code. Tech. rep. Technical Report AWRE/44/92/35.

Zhang, W., Wang, Z., 2015. Heat transfer enhancement of spray cooling in straight-grooved surfaces in the non-boiling regime. Exp. Therm. Fluid Sci. 69, 38–44. http://dx.doi.org/10.1016/j.expthermflusci.2015.08.001.

Zou, L., Wang, H., Zhu, X., Ding, Y., Liao, Q., 2023. The optimally chemically striped surface promotes the generation of larger satellite droplets. Colloids Surfaces A: Physicochem. Eng. Asp. 656, 130360. http://dx.doi.org/10.1016/j.colsurfa.2022.130360.